Research Article

Multiple ballistic impacts on 2024-T4 aluminum alloy by spheres: Experiments and modelling

J.C. Cheng[a], S.P. Zhao[b], D. Fan[b], H.W. Chai[b], S.J. Ye[a], C. Li[a], S.N. Luo[a], Y. Cai[b,*], J.Y. Huang[a,*]

[a] School of Materials Science and Engineering, Southwest Jiaotong University, Chengdu, Sichuan, P. R. China
[b] The Peac Institute of Multiscale Sciences, Chengdu, Sichuan, P. R. China

ARTICLE INFO

ABSTRACT

Multiple ballistic impacts are carried out on a 2024-T4 aluminum alloy by spherical steel projectiles (5-mm diameter) at ∼400 m s^{-1}, to investigate its dynamic deformation and damage. The ballistic impact process is captured with high-speed photography. Postmortem samples are characterized with optical imaging, three-dimensional laser scanning, microhardness testing and electron backscatter diffraction. With increasing number of impacts, crater diameter increases slightly, but crater depth and crater volume increase significantly, and strain accumulation leads to microhardness increase overall. Crater parameters all follow power-law relations with the number of impacts. Twin-like deformation bands and macroscopic deformation twins are produced by impact as a result of spontaneous dislocation self-pinning under high strain rate, large shear deformation. Under multiple impacts, shear strain accumulation in the arc-shaped region of the crater induces deformation twinning when it exceeds a critical value ($\sim 1.1 - 1.6$). It is highly possible that the deformation twins are related to deformation bands, since they both share one set of the {111} pole with the initial matrix grain. A finite element method model is optimized to reproduce experimental observations and interpret deformation mechanisms.

© 2021 Published by Elsevier Ltd on behalf of Chinese Society for Metals.

1. Introduction

Aluminum and its alloys have been widely used as structural materials in defense, aeronautics and aerospace industries, owing to their high specific stiffness and strength [1–4], and relatively low costs. Their excellent corrosion resistance also facilitates their use in some extreme environments [5]. However, accidental impact (e.g., bird strike or space debris) [6] on aluminum alloy structures is frequently encountered during service. Therefore, it is useful to investigate dynamic deformation and damage of aluminum alloys under impact or high rate loading, for the sake of safety assessment and structural design optimization.

Extensive investigations have been devoted to aluminum alloys under a wide range of strain rates, such as split Hopkinson bar loading [7,8], plate impact [9,10], laser shock [11,12], and ballistic impact [13–16]. Ballistic impact tests have been abundantly used to obtain the ballistic protective properties of a variety of materials [14,17] under various loading conditions, including different impact velocities [16] and projectile shapes [18]. However, studies on the multiple impact responses of materials are scarce [19,20]. Structures in aircrafts and armour may suffer attacks from a number of foreign objects, e.g., explosion-induced fragments, hail stones and space debris. Although such "projectiles" are launched randomly in time and space, there still exists possibility that structures are impacted repeatedly at the same or similar places by dense objects like bird flocks, massive fragments and debris cloud. A structure can survive a single impact, but may fail under repeated impacts. Impact cratering, deformation and damage of metal plates under multiple impacts are thus relevant to safety assessment and design optimization of key structures in service.

For instance, multiple (2–3) impacts were performed on ultra-high-performance concretes to investigate the effects of fiber reinforcement on their ballistic resistance [19]. The penetration depth of concrete targets was found to increase linearly with the number of impacts. Based on a single-impact penetration model, an empirical model was developed to predict the multiple impact penetration depth of semi-infinite concrete targets [20]. Nevertheless, previous repeated impact tests for metals such as aluminum alloys were all conducted with a drop weight system, at a velocity of only several meters per second [21–23]. Multiple impact tests at high velocities are essentially unexplored for alloys. Crater parameters (e.g., penetration depth and crater diameter) as a function of the number of impacts are required for validation of constitutive models, but are rarely addressed.

* Corresponding author.
   E-mail addresses: caiy@pims.ac.cn (Y. Cai), jyhuang_1989@163.com (J.Y. Huang).

Single ballistic impact experiments of aluminum alloys revealed such deformation and damage mechanisms as grain plasticity [14], recrystallization [15], adiabatic shear banding [24], microcrack/microvoid [13], and melting [25], depending largely on impact velocity, projectile shape and target plate thickness. A natural question is whether or not deformation/damage mechanisms are different under multiple impacts with similar incident energies. For instance, deformation twinning is highly unlikely in aluminum alloys under conventional loading given their face-centered cubic structure and high stacking fault energies (SFEs) [26,27]. However, macroscopic deformation twins (DTs) in single-crystal aluminum were found in dynamic equal channel angular pressing (D-ECAP) [28]. During such high strain rate shear, spontaneous self-pinning of dislocations impedes dislocation motion, and thus deformation twinning occurs under large shear deformation ($\sim$200%) at high strain rates ($\sim 10^6$ s^{-1}) [28]. Nanotwins were observed in a 7055 aluminum alloy impacted by a heavy tungsten alloy projectile at 1250 m s^{-1} [29]. However, macroscopic deformation twinning has not been reported in aluminum alloys under ballistic impact. Whether deformation twinning occurs in aluminum alloys subjected to high-speed multiple impacts, and how if it does, remain unsettled. Numerical simulations can provide many microscopic insights (e.g., the kinetic origin of strain accumulation under repeated loading) into experimental observations [30–32], but are rarely done for multiple high-speed impacts.

In this work, multiple impact tests are carried out on a 2024-T4 aluminum (2024Al-T4) alloy with spherical stainless steel projectiles at $\sim$400 m s^{-1}, to investigate the accumulation of dynamic deformation and damage and the underlying mechanisms, under repeated loading. The ballistic impact process is captured by a high-speed camera. Postmortem samples after multiple impacts are characterized with optical imaging, three-dimensional (3D) laser scanning, microhardness testing and electron backscatter diffraction (EBSD). The crater parameters are obtained as a function of the number of impacts, as well as the evolution of deformation mechanisms including deformation twinning. A finite element method (FEM) model is established for multiple high-speed impacts on the 2024Al-T4 alloy against the experiments, and used to help interpret experimental observations.

2. Experiments

2.1. Materials

The 2024Al-T4 alloy is received as an as-rolled plate commercially produced by Aleris. The chemical composition (wt.%) of the 2024Al-T4 alloy is Cu: 4.14, Mg: 1.48, Mn: 0.55, Fe: 0.19, Si: 0.15, Zn: 0.11, Ti: 0.05, Cr: 0.03, and Al: balance. The 2024Al-T4 alloy has a bulk density $\rho_0 = 2.78$ g cm^{-3} as measured with the Archimedean method. The longitudinal (C_L) and transverse (C_T) sound velocities obtained from ultrasonic measurements are 6170 m s^{-1} and 3190 m s^{-1}, respectively. The bulk sound velocity (C_B) and Poisson's ratio (ν) are calculated from C_L and C_T are $C_B = 4950$ m s^{-1} and $\nu = 0.32$, respectively.

Initial EBSD characterizations on the as-received materials are presented in Fig. 1(a–c). Only grain boundaries with a misorientation angle greater than 10° are marked in black (the same below). The grains are elongated along the rolling direction (RD), a typical feature for rolled plates. The grain size along the RD (Fig. 1(b)) is greater than 1.5 mm. The average grain size is $\sim$300 m and $\sim$100 m along the transverse direction (TD) and the normal direction (ND), respectively. The white substances in Fig. 1(d–f) are the precipitate phases (mainly Al_2Cu, Al_2CuMg, $Al_{20}Cu_2Mn_3$, and Al_7Cu_2Fe [33].), which are more densely distributed in the ND-TD and ND-RD planes than in the TD-RD plane. The precipitate phase distributions in the ND-TD and ND-RD planes appear ran-

dom, while the precipitate phases are distributed intermittently along the RD in the ND-RD plane. The precipitate phases are distributed at grain boundaries and inside grains, consistent with previous observations [10]. The kernel average misorientation (KAM) map (Fig. 1(b) inset) indicates nearly zero misorientations across the sample, and thus negligible residual strains in the as-received material.

2.2. Ballistic impact experiments

Ballistic impact experiments are conducted on a single-stage gas gun with a bore diameter of 14 mm [34]. The schematic configuration for the ballistic impact experiments is presented in Fig. 2(a). A spherical projectile (4) is attached to the front end of an aluminum sabot (3). When the solenoid valve is fired, high pressure helium or nitrogen gas stored in a reservoir is released into the gun barrel (2) to accelerate the sabot and projectile assembly. The sabot velocity is measured with an electromagnetic induction velocimeter (5) upon exiting the gun barrel, which also sends a trigger signal to the high-speed camera (10). The sabot is then stopped by a block (6) with a hole of 10-mm diameter, while the projectile is separated from the sabot and continues to fly and then impacts the 2024Al-T4 alloy target (7) which is supported with the sample/target holder (8). This sample/target holder (8) is fixed to the chamber (1). The high-speed camera is set perpendicular to the ballistic impact direction, and the contact surface between projectile and target is in the middle of the field of view. The lighting (11) is kept on throughout the experiment. A polarizer is mounted in front of the high-speed camera to filter the flash upon the initial impact. The uncertainties in the sabot velocity measurements are about 1%.

The spherical projectiles are made of 304 stainless steel with a diameter of 5 mm, a density of 7.93 g cm^{-3}, and a mass of about 0.52 g. Five samples (samples 1–5) are used as targets, and are subjected to 1–5 times of impact, respectively (15 shots in total). All the target samples have the same dimensions of 100 mm $\times$ 100 mm $\times$ 50 mm (thickness 50 mm), and are harvested from the same plate (1,600 mm $\times$ 3,660 mm $\times$ 50 mm). A thick block sample allows for studying multiple impacts with minimum boundary effects. Thick plates have been widely used in fortifications and armour, and their ballistic impact response is of interest as well [13–15]. During ballistic impact experiments, the spherical projectiles are launched along the ND, perpendicular to the impact surface, at an impact velocity of $\sim$400 m s^{-1}. Multiple impacts are performed under the same experimental conditions. The projectile impact and rebound process are captured by the high-speed camera at 100,000 frames per second. The projectile and crater parameters are defined in Fig. 2(b). d_p is projectile diameter (black). d_c, D_c and V_c are diameter, depth and volume of the crater (blue), respectively. Microhardness tests are performed in postmortem samples along two line segments, *AB* and *CD*.

2.3. Microstructural characterizations

Postmortem samples recovered from ballistic impact experiments are characterized with optical imaging, 3D laser scanning, microhardness testing, and EBSD. The craters are scanned by a 3D laser scanner (PRINCE 335, Hangzhou Scantech Co., Ltd.) at a scanning rate of 320,000 per second to obtain the 3D surface grid data. A blue laser serves as the light source of the 3D scanner. All the samples are then sliced with electrical discharge machining. The cutting surface is parallel to the RD - ND plane and passes through the crater center. The cut surface is ground and polished with 1 m and 0.3 m alumina particles. Vickers microhardness is measured with a microhardness tester manufactured by Laizhou Huayin Testing Instrument Co., Ltd. The load is 0.2 kg, and the dwell time is
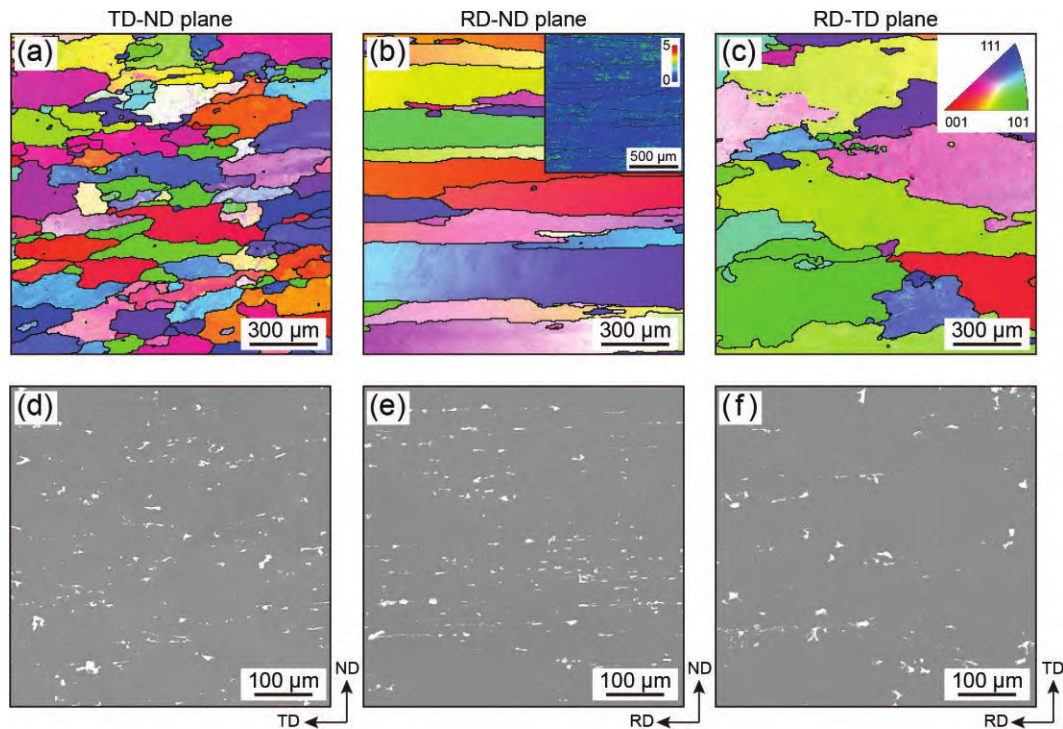
Fig. 1. Microstructural characterizations on the as-received 2024Al-T4 alloy. (a)–(c) Inverse pole figure (IPF) maps. Inset of (b): kernel average misorientation (KAM) map. EBSD scan step size: 4.73 m. (d)–(f) Backscattered electron images. White areas refer to precipitates. RD: rolling direction; TD: transverse direction; ND: normal direction.
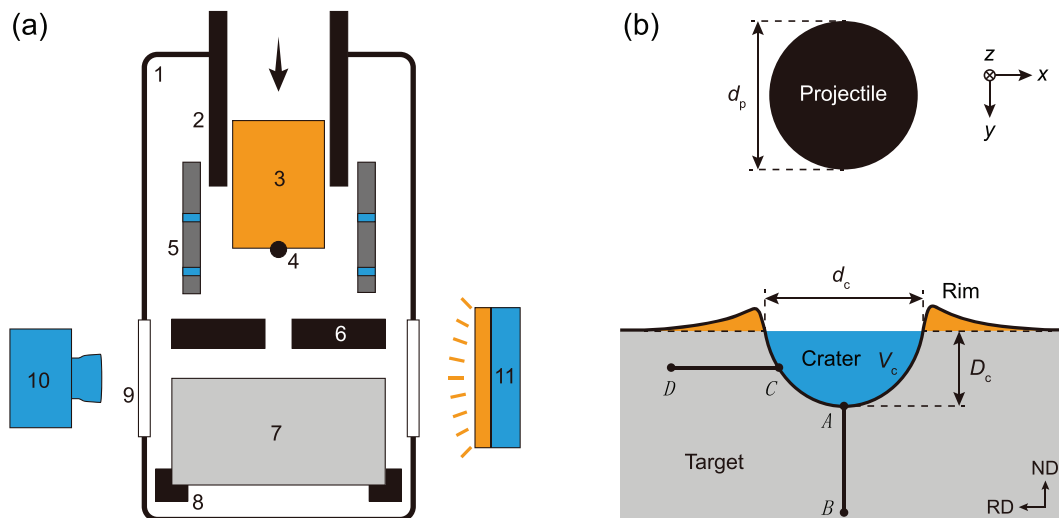

Fig. 2. (a) Schematic setup for ballistic impact experiments. 1: target chamber; 2: gun barrel; 3: aluminum sabot; 4: spherical projectile; 5: electromagnetic induction velocimeter; 6: steel block; 7: 2024Al-T4 alloy target; 8: target holder; 9: polycarbonate windows; 10: high-speed camera; 11: light. (b) Definition of experimental parameters. d_p: projectile diameter; d_c: crater diameter; D_c: crater depth; V_c: crater volume.

15 s. Prior to EBSD characterizations, grinding and polishing are applied to the cutting surface, followed by electropolishing in a solution of 10 vol.% perchloric acid and 90 vol.% ethanol at 25 V and −25°C using a Cu rod and the sample as electrodes. EBSD characterizations are performed with an FEI Quanta 250 SEM with an Oxford EBSD detector. More details on EBSD were presented elsewhere [34].

2.4. FEM Modeling

As shown in Fig. 3, a 2D axisymmetric finite element model (4-node brick elements) of a 2024Al-T4 alloy target and a spherical projectile are constructed. The 2024Al-T4 alloy target has dimensions of 100 mm × 50 mm. Fine elements (0.25 mm × 0.25 mm) are used in the center region, coarser elements (1 mm × 1 mm) are used for the peripheral regions, and medium elements (0.5 mm × 0.5 mm) are used between the fine and coarse elements (Fig. 3). Ballistic impact induces large deformation, including compression, tension and shear, which can cause mesh distortion. Therefore, the arbitrary Lagrangian-Eulerian method [35] is adopted. The left and right sides of the 2024Al-T4 alloy plate are fixed; air layers of 20 mm and 10 mm thickness are placed on the top and bottom of the target, respectively. The density of air is set as 1.29 kg m^{-3}. The steel projectile with a 5-mm diameter is treated as a rigid body given its minor deformation during impact.
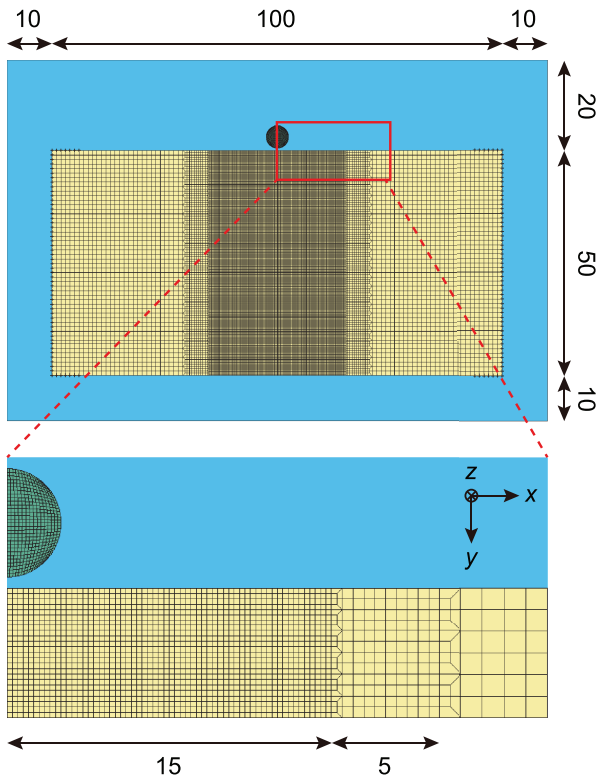
Fig. 3. Geometry and meshing of the 2024Al-T4 alloy target and stainless steel projectile. Dimensions are in millimeters.

Table 1
Material parameters for FEM simulation. ρ_0: initial density; ν: Poisson's ratio; E: Young's modulus; σ_0: static yield stress; E_t: tangent modulus; β: strain hardening parameter; C and P: strain-rate related parameters.

ρ_0 (g cm^{-3})	ν	E (GPa)	σ_0 (GPa)	E_t (GPa)	β	C (s^{-1})	P
2.78	0.32	71	0.29	0.51	1	6.0×10^6	4.5

A typical model incorporating strain rate effects, the Cowper-Symonds material model [36], is adopted here for describing the mechanical behavior of the 2024Al-T4 alloy target under ballistic impact. In this elastic-plastic constitutive model, the yield strength as a function of effective plastic strain ($\varepsilon_{\mathrm{eff}}^{\mathrm{p}}$) and strain rate ($\dot{\varepsilon}$), is written as

$$\sigma_{\mathrm{y}} = \left(\sigma_0 + \beta E_{\mathrm{p}}\varepsilon_{\mathrm{eff}}^{\mathrm{p}}\right)\left[1 + \left(\frac{\dot{\varepsilon}}{C}\right)^{\frac{1}{P}}\right], \quad (1)$$

where σ_0 is the initial yield stress, β is the strain hardening parameter, C and P are the Cowper-Symonds strain rate parameters, and E_{p} is the plastic hardening modulus.

E_{p} is described in terms of the elastic modulus, E, and the tangent modulus, E_{t}, as follows

$$E_{\mathrm{p}} = \frac{EE_{\mathrm{t}}}{E - E_{\mathrm{t}}}. \quad (2)$$

Material parameters for the 2024Al-T4 alloy target used in the FEM simulation are listed in Table 1. The Young's modulus (E) and the initial yield strength (σ_0) of the 2024Al-T4 alloy are obtained from the quasi-static (strain rate 0.001 s^{-1}) tensile test as $E = 71$ GPa and $\sigma_0 = 0.29$ GPa. The tangent modulus (E_{t}) is calculated as the average slope of the real compression stress-strain curve at the plastic stage by linear fitting, and $E_{\mathrm{t}} = 0.51$ GPa. β is set as a typical value (1.0) in literature [37]. C and P are selected as 6×10^6 s^{-1} and 4.5, respectively, to fit the experimental results.

Table 2
Impact velocity (v_{i}) and rebound velocity (v_{r}) of the projectile for different impacts, both in m s^{-1}.

Impact	Sample 1		Sample 2		Sample 3		Sample 4		Sample 5	
	v_{i}	v_{r}	v_{i}	v_{r}	v_{i}	v_{r}	v_{i}	v_{r}	v_{i}	v_{r}
1st	391	51	393	51	399	52	395	52	393	51
2nd	–	–	393	65	393	63	396	65	398	64
3rd	–	–	–	–	391	61	392	68	396	66
4th	–	–	–	–	–	–	398	65	398	65
5th	–	–	–	–	–	–	–	–	393	67

3. Results and discussion

Ballistic impact experiments are carried out for 2024Al-T4 alloy at ~400 m s^{-1}. Snapshots of a steel projectile impact on a 2024Al-T4 alloy target during the first impact are shown in Fig. 4, which allow for the evaluation of projectile velocities at different stages. The steel projectile impacts into the target, creating a crater, and then rebounds. We define time zero ($t = 0$) as the moment when the projectile is first in contact with the front surface of the 2024Al-T4 alloy. At this point, a flash from the impact surface can still be seen even with the polarizer in place. At $t = 10$ μs, the projectile invades the target, and only about half the projectile is visible. The velocity of the projectile drops rapidly to zero and then becomes negative (rebound). Meanwhile, debris is ejected from the impact surface at ~10 m s^{-1} (the black arrows).

A sample is subjected to one or multiple repeated impacts. In the following discussion, sample i refers to the sample subjected to i repeated impacts. The corresponding projectile impact and rebound velocities are listed in Table 2. The rebound velocity is ~50 m s^{-1} for the first impact, and then increases to ~65 m s^{-1} for multiple impacts.

3.1. Macroscopic measurements on impact craters

3.1.1. Morphology analysis

Crater morphology changes for different numbers of impacts. With increasing number of impacts, the crater inner wall becomes darker (Fig. 5(a)). Cracks are not observed at the crater rim tip for sample 1, but for samples 2–5 (marked by the red arrows); such cracking is the most pronounced for sample 5. In order to further analyze crater morphology, 3D laser scanning is applied to obtain surface grid data of craters. The 3D renderings of craters seen from different perspectives are presented in Fig. 5(b–c). The crater rim tips of all samples are uneven (Fig. 5(b)), probably due to heterogeneous local plastic flow and damage. The crater depth and volume increase significantly with the increase of impact times (Fig. 5(c)).

The 3D images are analyzed to extract the cross-sectional profile and morphology parameters (crater depth D_{c}, crater diameter d_{c} and crater volume V_{c}) of craters. Given the surface grid data, the plane far from the crater is identified as the impact surface. The material phase and air phase are distinguished in reference to the impact surface. The crater is defined as the air phase below the impact surface, while the rim is the material phase above the impact surface. Thus, V_{c} can be calculated as the volume summation of void pixels below the impact surface. The impact axis (perpendicular to the impact surface) is determined precisely from a 3D image. Then, a cylindrical coordinate system ($r - \theta - y$) is established, and its origin is at the intersection point of the impact axis with the impact surface. Here, r is the radial length, θ is the azimuthal angle ranging from 0 to 2π, and the y-axis coincides with the impact axis. For each θ, a $y - r$ curve can be obtained, and averaging such curves for different θ values yields the cross-sectional profile of the crater for each sample.
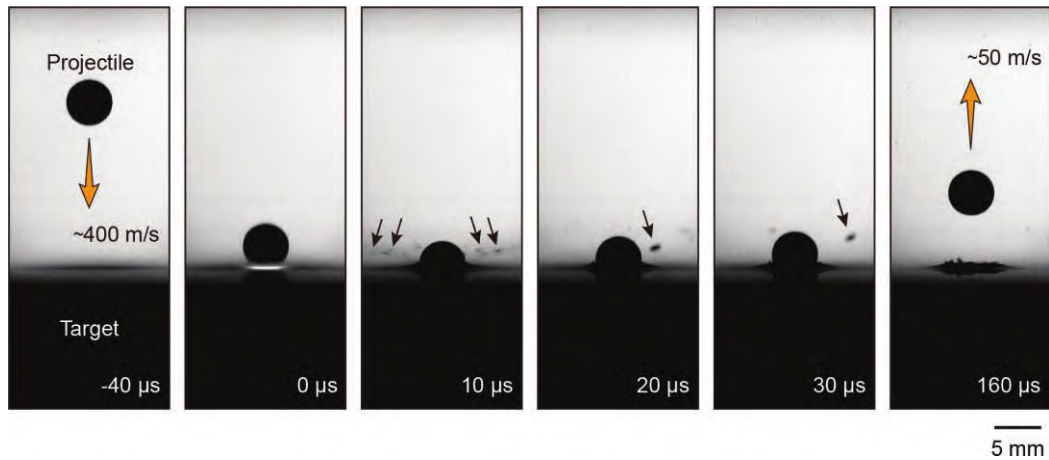
Fig. 4. Snapshots of a steel projectile impacting on a 2024Al-T4 alloy target (sample 1) at ~400 m s^{-1}.
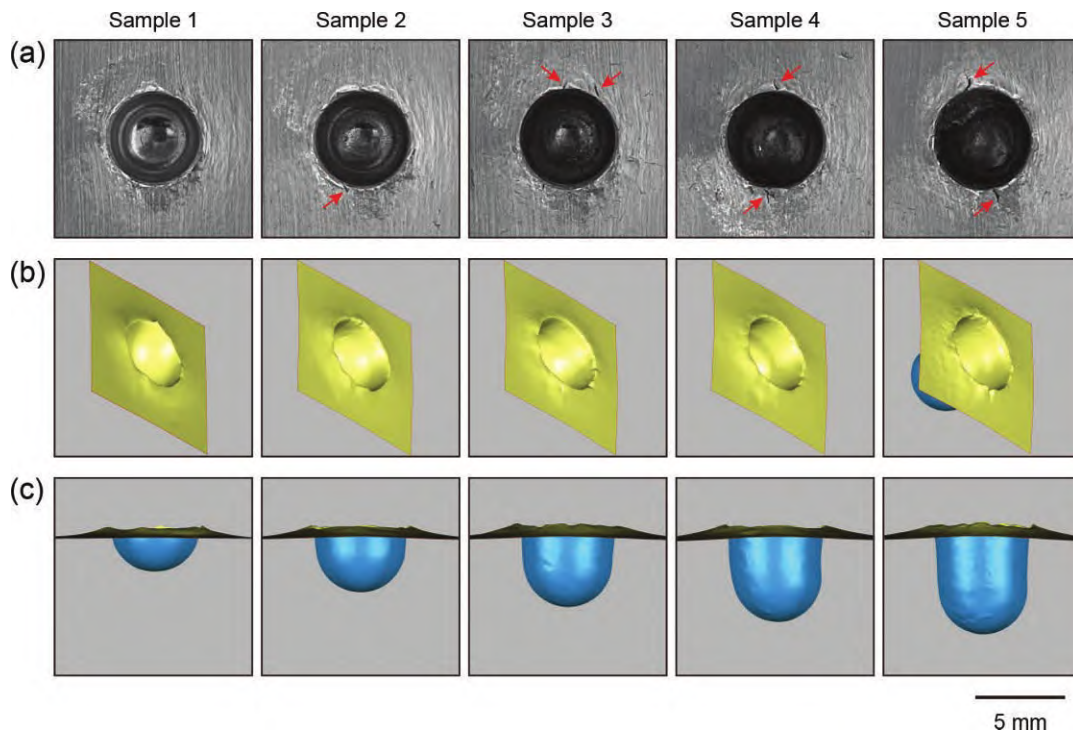

Fig. 5. (a) Optical images of the postmortem samples impacted along the ND for 1–5 times (samples 1–5). (b)–(c) 3D laser scanning reconstruction of the impact craters viewed from different perspectives.

Cross-sectional profiles of the craters are presented in Fig. 6 for the five samples, with representative error bars. For each curve, the segments below and above $y = 0$ represents crater and rim, respectively. The average standard deviation over the five samples is small (0.095 mm), indicating that the craters are approximately rotationally symmetric with respect to the impact axis. The standard deviation near the highest point of a curve (the rim tips) is relatively large due to the presence of microcracks, consistent with Fig. 5(a) (marked by the red arrows).

The crater parameters, D_c, d_c and D_c/d_c for the 1st to 5th impacts are extracted and presented in Fig. 7(a). For the 1st impact, D_c is less than half of the projectile diameter, and d_c is less than the projectile diameter (5 mm). With increasing number of impacts, d_c increases slightly, while D_c increases rapidly from 1.9 mm to 5.1 mm. This results in an increase in the crater shape parameter from 0.38 to 0.96. The crater shape changes from a hemisphere

to a spherical-nosed cylinder. Similarly, V_c expands markedly with the increasing number of impacts (Fig. 7(b)).

3.1.2. Analytical analyses

The shock pressure (P_i) at the instant of impact in the 2024Al-T4 alloy target can be calculated according to the one-dimensional shock wave theory [6], while the so-called stable-state pressure (P_s) at the crater bottom can be obtained according to the momentum conservation equation [38]:
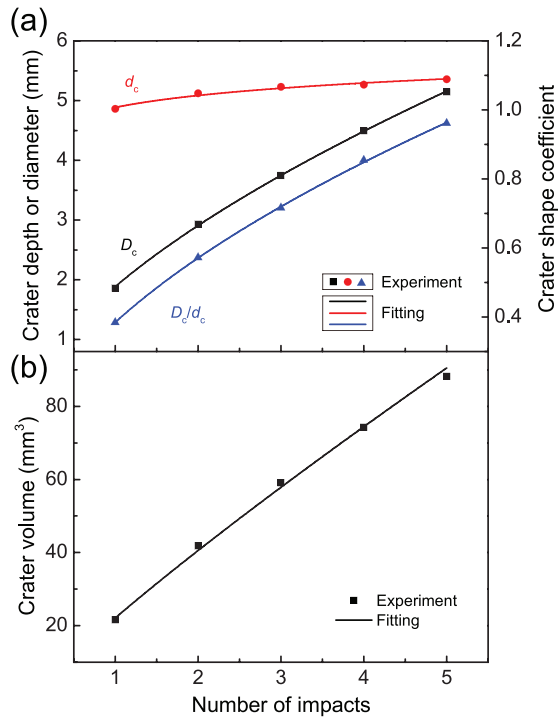
$$P_i = \rho_0 (C_B + SU_p)U_p, \tag{3}$$

$$P_s = \frac{1}{2}\left[\rho_0\rho_p\left(\rho_0^{\frac{1}{2}} + \rho_p^{\frac{1}{2}}\right)^{-2}\right]v_i^2, \tag{4}$$

where ρ_0 and ρ_p are the densities of the 2024Al-T4 alloy and the projectile, respectively. C_B is the bulk sound velocity, and $S = 1.29$
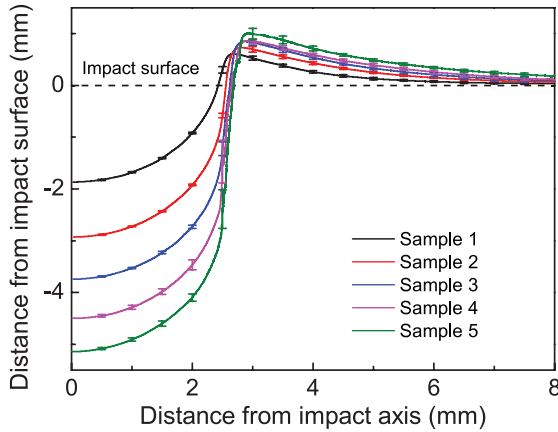
Fig. 6. Cross-sectional profiles of the craters after 1–5 impacts (samples 1–5). The original plane refers to the target surface prior to impact.


Fig. 7. (a) Depth (D_c), diameter (d_c), shape coefficient (D_c/d_c) and (b) volume (V_c) of craters as a function of the number of impact. Symbols: experimental data; lines: fitting to data with a power function.

is a material constant [39] for the 2024Al-T4 alloy. The particle velocity (U_p) of the 2024Al-T4 alloy calculated by the impedance match method [40] is ~290 m s^{-1} for the projectile velocity $v_i \approx$ 400 m s^{-1}. P_i and P_s are calculated as 4.3 GPa and 90 MPa, respectively. P_i is higher than P_s by one order of magnitude, since P_i drops rapidly with time.

Power-law relations have been observed between crater parameters and incident kinetic energy (E_k) in single ballistic impact: $Y = aE_k^b$ [41,42], where a is a fitting parameter, b is the exponent, and Y can be D_c, d_c, D_c/d_c or V_c. Multiple impacts represent a different type of energy input. In our experiments, E_k for each impact is a constant (~40 J). The crater parameters Y after multiple impacts can also be described with a power function as

$$Y = a(nE_k)^b = \eta n^b, \tag{5}$$
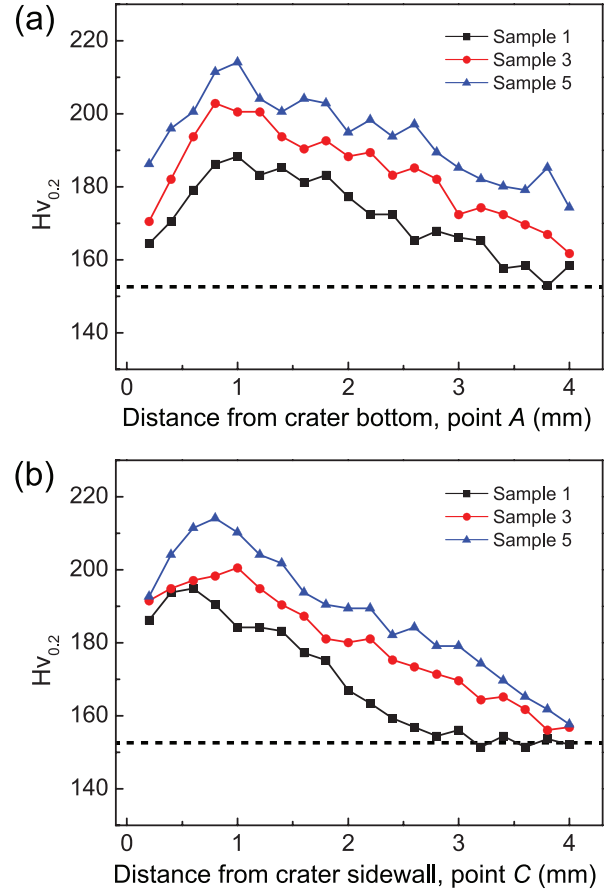
Fig. 8. Microhardness distributions along the two lines marked in Fig. 2(b) for samples 1, 3, and 5. Hv$_{0.2}$ refers to the Vickers hardness under a load of 0.2 kg. Dashed lines: the as-received sample.

where n is the number of impacts, and η is a fitting parameter (normalization factor). Fig. 7 shows that the experimental data can be described well with the power laws with the following parameters: $\eta = 1.886 \pm 0.015$ mm, $b = 0.625 \pm 0.006$ for D_c; $\eta = 4.885 \pm 0.027$ mm, $b = 0.058 \pm 0.005$ for d_c; $\eta = 0.384 \pm 0.003$, $b = 0.571 \pm 0.006$ for D_c/d_c; $\eta = 22.100 \pm 1.080$ mm^3, $b = 0.876 \pm 0.035$ for V_c. In particular, the small exponent for d_c indicates that d_c is insensitive to the number of impacts. Such power-law relations can help evaluate service safety and optimize structural design of protection structures under multiple impacts.

Adiabatic heating during ballistic impact leads to a temperature rise ΔT, which can be calculated as [43]

$$\Delta T = \frac{\varphi \int \sigma_{eff} d\varepsilon_{eff}^p}{\rho_0 C_v}. \tag{6}$$

Here σ_{eff} and ε_{eff}^p are effective stress and effective plastic strain, respectively. ρ_0 is density. C_v is specific heat capacity at constant volume. φ is the fraction of plastic work converted into heat, referred to as the Taylor-Quinney parameter, and $\varphi = 0.4$ for the 2024Al-T4 alloy [44]. The plastic work in Eq. (6) is obtained from the FEM simulation.

3.2. Microscopic characterization of postmortem samples

Bulk impact properties depend on the number of impact, while deformation and damage may vary at different locations around a crater. We explore next the related microscopic features via microhardness and EBSD characterizations of the postmortem samples.
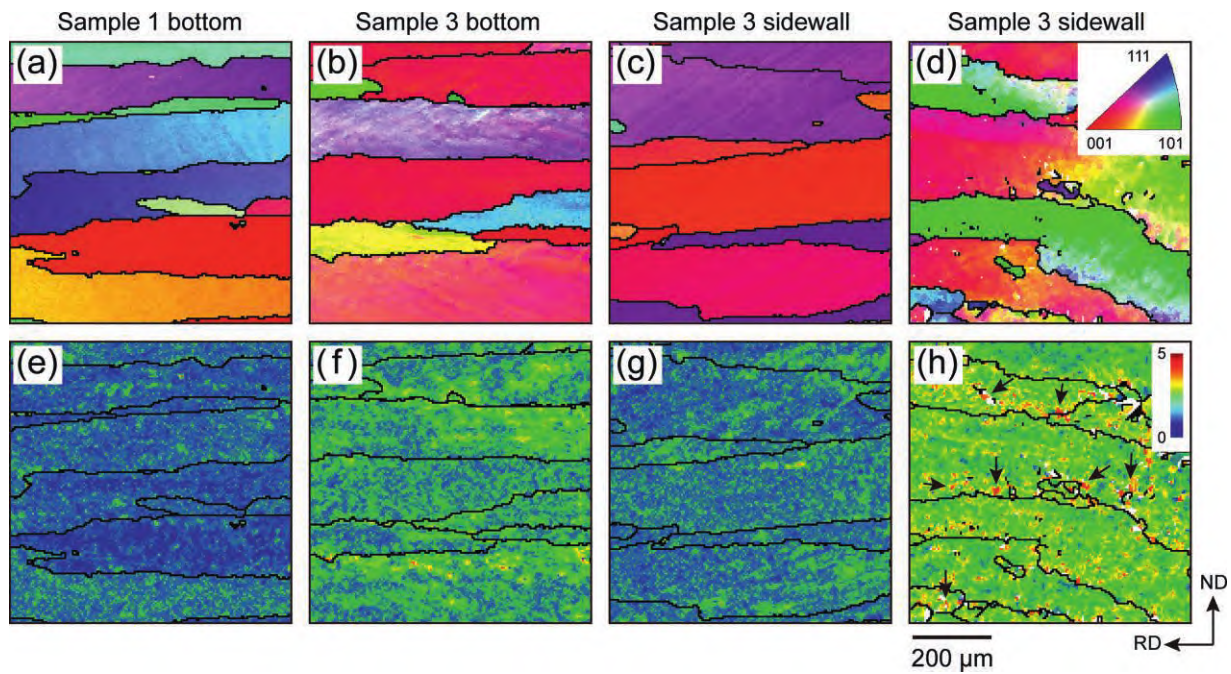
Fig. 9. EBSD characterizations of the postmortem samples. (a)–(d) IPF maps for samples 1 and 3. The centers of maps (a) and (b) lie on the line *AB* (Fig. 2(b)), and are 4 mm away from point *A* (crater bottom). The centers of maps (c) and (d) lie on the line *CD* (Fig. 2(b)), and are 4 mm and 1 mm away from point *C* (crater sidewall center), respectively. (e)–(h) KAM maps corresponding to maps (a)–(d). EBSD scan step size: 4.73 m.

3.2.1. Microhardness

Microhardness testing is conducted along two line segments *AB* (crater bottom) and *CD* (crater sidewall) indicated in Fig. 2(b). Microhardness refers to the Vickers hardness under a load of 0.2 kg, denoted as $Hv_{0.2}$, and the results are shown in Fig. 8. For the as-received 2024Al-T4 alloy, $Hv_{0.2}$ is 152.6 ± 3.6 (the dashed lines). The impacts induce an overall increase in microhardness in all cases. However, microhardness increases within a narrow range (∼1 mm) and reaches the maximum, and then decreases with increasing distance. The lower values (than expected) in this narrow region is probably resulted from damage near the crater [45], while decreasing plastic strain (and strain hardening) at further distances results in the drop from the maximum hardness [46].

The first impact leads to an overall increase in microhardness within a ∼3.8 mm region from the crater bottom along the impact direction (Fig. 8(a)), but within a lesser range (∼2.8 mm) from the crater sidewall perpendicular to the impact direction (Fig. 8(b)). With increasing number of impacts, the maximum microhardness increases and the affected range widens, as a result of the accumulation of plastic strain during multiple impacts. The plastic strain accumulation also leads to a reduced rate of increase in D_c (Fig. 7(a)).

3.2.2. Plastic deformation around the crater

Fig. 9 shows the IPF maps and corresponding KAM maps at different positions for sample 1 and sample 3. Compared to the as-received sample (Fig. 1(b)), the grain morphology remains approximately unchanged in the regions 4 mm away from the crater edges (Fig. 9(a–c)). However, the corresponding KAM maps show obvious differences (Fig. 9(e–g)). For sample 1, the KAM map in the region 4 mm away from the crater bottom (Fig. 9(e)) is similar to that of the as-received sample (Fig. 1(b) inset), consistent with the microhardness measurements (Fig. 8(a)). However, the KAM map of sample 3 in the same region shows a considerable increase in KAM values compared to sample 1, leading to a higher strain hardening of materials. In contrast to Fig. 9(c), grains in the region ∼1 mm away from the crater sidewall exhibit obvious bending along the
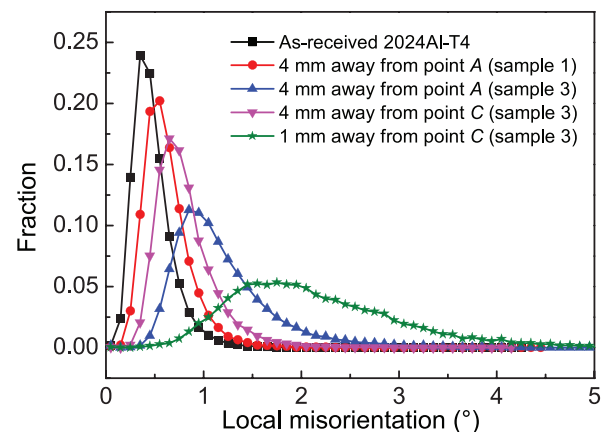

Fig. 10. Local misorientation distributions of the as-received and postmortem samples (samples 1 and 3) at different positions.

tangential direction of sidewall (Fig. 9(d)). Grain orientations also change considerably, for example, from ⟨001⟩ to ⟨101⟩. The local misorientation angles (Fig. 9(h)) are appreciably higher than those in the far-field regions. In addition, a large number of high-KAM-value spots (marked by the arrows) are observed across the sample in Fig. 9(h). Such KAM spots normally correspond to local strain concentrations [47], and are probably induced by strain accommodation at the precipitate-matrix interfaces (Fig. 1(d–f)) due to their modulus mismatch [48,49]. The precipitate-matrix interfaces tend to serve as nucleation sites of dislocations.

The local misorientation distributions calculated from Fig. 9(e–h) and Fig. 1(b) inset are shown in Fig. 10. The local misorientation of the as-received 2024Al-T4 alloy shows a narrow distribution between 0° and 1°. The average of local misorientations is 0.48° with a standard deviation of 0.22°. The misorientation distributions of samples after impact shift toward larger local misorientation. In the same region (4 mm away from the crater bottom), the average
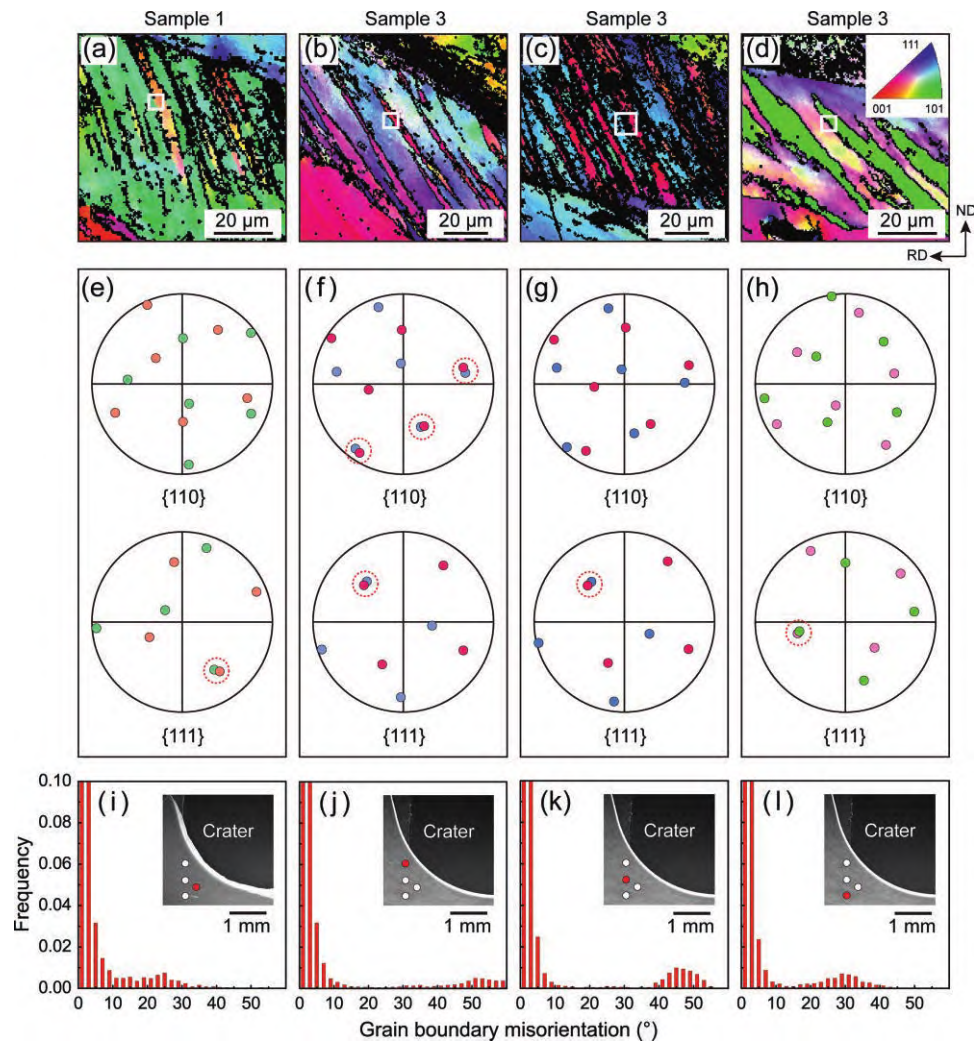
Fig. 11. (a)–(d) EBSD characterizations of the impact-recovered samples. Unindexed areas and grain boundaries with misorientation greater than 10° are marked in black. EBSD scan step size: 0.5 m. (e)–(h) {110} and {111} pole figures corresponding to the regions indicated by white rectangles in (a)–(d). (i)–(l) Grain boundary orientation distribution corresponding to (a)–(d). Insets of (i)–(l) display the positions of EBSD characterizations (red dots) for (a)–(d). (For interpretation of the references to colour in this figure legend, the reader is referred to the web version of this article.)

local misorientation of sample 3 (1.19°) is considerably larger than that of sample 1 (0.62°), as a result of plastic strain accumulation. However, for the same sample 3, local misorientations at the bottom region are statistically larger than those at the sidewall region (0.81° in average). Therefore, plastic deformation extends deeper into the crater bottom region along the impact direction. This explains why microhardness decreases more slowly along this direction (Fig. 8). As expected, the average local misorientation at the region 1 mm away from the crater sidewall is the largest (2.12°) among all the five regions. In addition, the local misorientation distribution in this case shows a very long decay detail due to the existence of high-KAM-value spots, resulting in the biggest standard deviation (0.82°).

3.2.3. Deformation banding and twinning

Interestingly, twin-like structures (lens-shaped grains) are observed in the region adjacent to the spherical nose of the crater (less than 1 mm away from the crater edge) in the postmortem samples 1 and 3 (Fig. 11). However, no such structures are observed in the bottom area (not shown). The precise locations for EBSD characterization in Fig. 11(a–d) are marked by red dots in the insets of Fig. 11(i–l). The corresponding {110} and {111} pole figures of the local twin-like structures (marked with white rectangles in Fig. 11(a–d)) are presented in Fig. 11(e–h), along with

the corresponding grain boundary (GB) misorientation distributions shown in Fig. 11(i–l). The minimum misorientation angle of the grain boundaries is 1° for the statistics.

For sample 1, the lens-shaped grains share one set of the {111} pole with the initial matrix grain (marked by a dashed circle in Fig. 11(e)); however, coincidence of any ⟨110⟩ directions is not observed in the {110} pole, different from the pole figure of twins [50]. Therefore, such structures in sample 1 are called twin-like deformation bands (DBs), which were previously observed in aluminum under D-ECAP [50,51], and aluminum alloys [29,52] and 304L stainless steel [38] under single ballistic impact. The corresponding GB misorientation distribution (Fig. 11(i)) shows that the misorientations of GBs are mainly distributed in 15° − 30°.

In the pole figure of sample 3 at the region closest to the crater edge (Fig. 11(f)), the crystallographic relationship between the lens-shaped grains and the initial matrix grain exhibits coincidence of three pairs of ⟨110⟩ directions and one pair of ⟨111⟩ directions (marked by the dashed circles in Fig. 11(f)). Furthermore, Fig. 11(j) shows that the misorientations of GBs are mostly located in 50° − 60°. These results confirm that the lens-shaped grains follow a twin orientation relationship with the initial matrix grain [50]. In other words, macroscopic deformation twins (DTs) are produced in sample 3. The maximum twin width is about 7 m while the twin length is close to 100 m. Similarly, macroscopic DTs were

discovered in a single-crystal Al [28] and a polycrystalline 6061Al alloy [53] under D-ECAP. At a greater distance from the crater edge, however, the GB misorientations decrease to $40° − 50°$ (Fig. 11(k)), but are significantly higher than those in sample 1 at a similar location of EBSD characterization. In addition, the GB misorientations of twin-like DBs decrease with increasing distance from the crater edge (Fig. 11(j–l)), while their pole figures all show coincidence of one pair of $\langle 111 \rangle$ directions. This indicates that the DBs are probably formed by way of gradual lattice rotation around the rotation axis $\langle 111 \rangle$.

During multiple impacts, the deformation modes in the 2024Al-T4 alloy change with strain accumulation. Only twin-like DBs appear in the sample at the first and second impacts. After the third impact, twin-like DBs and macroscopic DTs coexist, inducing pronounced strain hardening. Therefore, the impact resistance of the 2024Al-T4 alloy increases considerably with increasing number of impacts, leading to a descending increasing rate of D_c (Fig. 7).

Such macroscopic DTs are observed for the first time in ballistic impact experiments, especially in high-SFE Al and its alloys. In general, dislocation slip is the main deformation mode during impact cratering of Al alloys [14]. In fact, only deformation bands form via dislocation slip during the first two impacts. High-rate shear strain accumulates with increasing number of impacts, which is the thermomechanical origin [54] of dynamic deformation under repeated loading. However, dislocation self-pinning and tangling, as well as DBs formed during previous impacts, impede dislocation motion and give rise to intense shear stress accumulation and subsequently deformation twinning [28] in order to accommodate the large strain. Twin-like DBs become an important supplement in such extreme plastic deformation cases. This describes the primary kinetic origin [55–57] of dynamic deformation accumulation. It is highly possible that the deformation twins are related to deformation bands, since they both share one set of the {111} pole with the initial matrix grain [58]. However, the exact nature of their relation remains to be revealed with thermomechanical calculations [54,59], molecular dynamics simulations and first-principles calculations [30,49], or advanced experiments.

3.3. FEM simulation

FEM simulations of multiple impacts on 2024Al-T4 alloy are performed to assist interpretation of our experimental observations. The steel projectile velocity is set at 400 m s^{-1}, and the rebound velocity is approximately the same as the experimental results: ∼50 m s^{-1} for the 1st impact and ∼65 m s^{-1} for the multiple-impact cases. The simulated P_i and P_s are ∼2 GPa and ∼100 MPa, respectively, consistent with the analytical analyses from Eqs. (3) and (4). Crater parameters, and velocity and strain fields are derived from FEM analyses. The simulated D_c and d_c values are shown in Fig. 12 as a function of the number of impacts, which agree well with the experimental results. The reduced rate of increase (the exponent in Eq. (5)) in crater depth with increasing number of impacts is attributed to strain hardening of 2024Al-T4 alloys induced by deformation banding and twinning. Sensitivity analyses on E_p show that the rate of increase for crater depth decreases considerably with increasing E_p. Therefore, the materials with higher strain hardening (e.g., titanium alloy, and stainless steel) are supposedly more resistant to multiple impacts.

The instantaneous velocity fields for samples 1 and 3 at different instants are demonstrated in Fig. 13. For the 1st impact at $t = 1$ μs, the velocity vectors are of the largest amplitude in sample region in contact with the projectile and oriented along the radial direction of the projectile. The velocity decays rapidly along this direction. Meanwhile, a crater rim begins to form at the impact surface adjacent to the crater, due to an upward plastic flow of materials. The crater volume and depth increase ($t = 2$ μs).
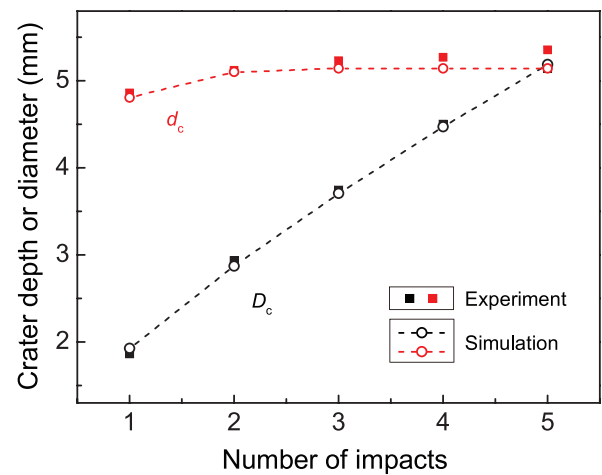

Fig. 12. Crater depth (D_c) and diameter (d_c) as a function of the number of impacts obtained from FEM simulations and experiments.
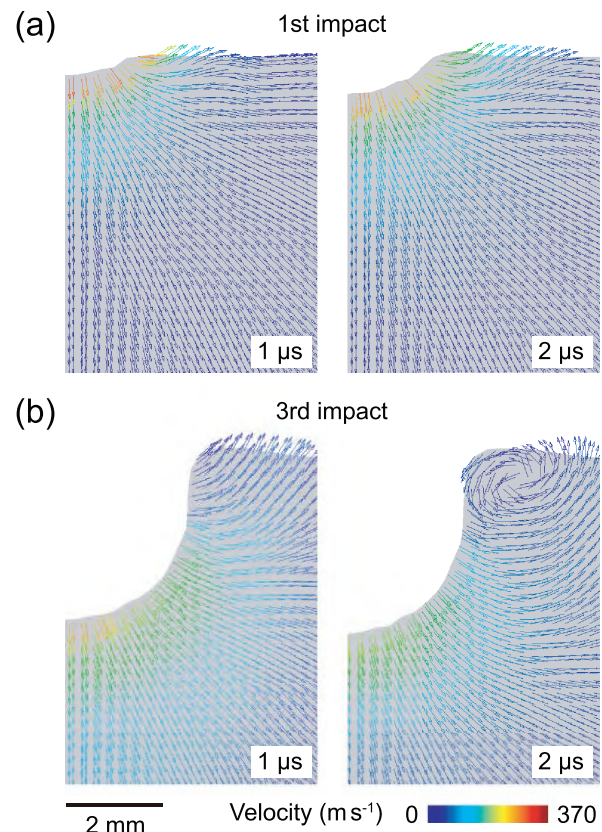

Fig. 13. FEM simulations: snapshots of instantaneous velocity fields of the 2024Al-T4 alloy targets after (a) the 1st impact and (b) 3rd impact.

The maximum velocity around the crater drops from 351 m s^{-1} to 329 m s^{-1}. The range of plastic flow increases, resulting in an increased volume of the rim. For the 3rd impact, the maximum velocity (307 m s^{-1}) is considerably lower than that for the 1st impact at $t = 1$ μs; it drops continually to about 248 m s^{-1} at $t = 2$ μs. Therefore, the deceleration for the 3rd impact is larger than that for the 1st impact, resulting in a shorter overall response time [21]. In addition, a whirlpool-like velocity vector field forms around the crater top at $t = 2$ μs for the 3rd impact, as a result of outward extrusion and downward tension. This explains why d_c
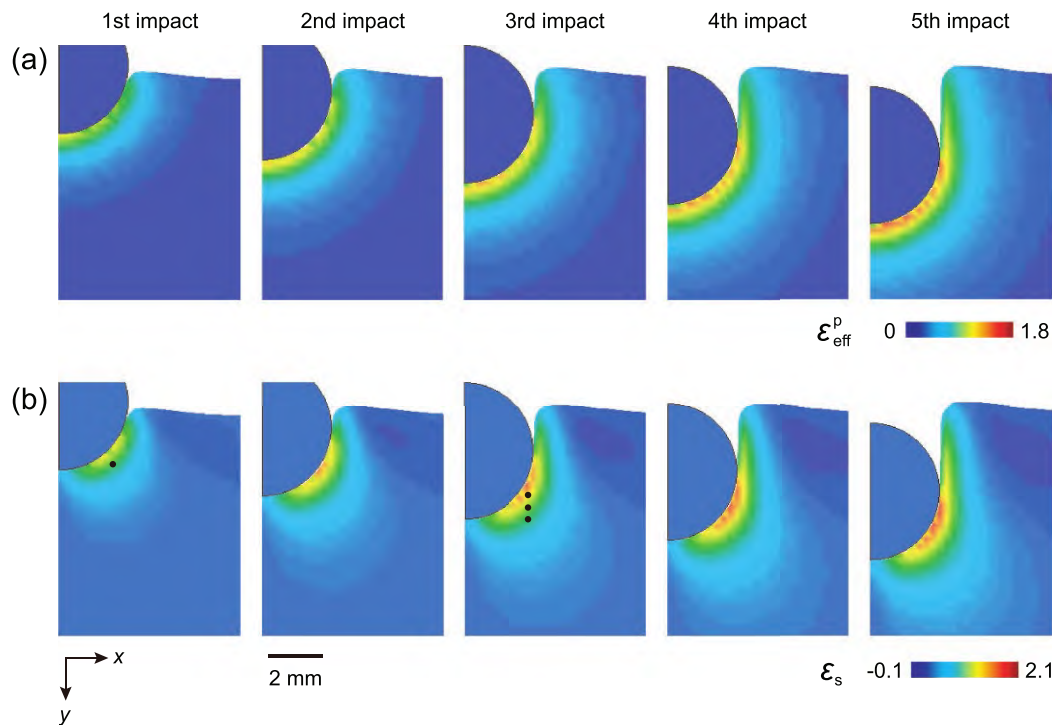
Fig. 14. Snapshots of instantaneous (a) effective plastic strain ($\varepsilon_{\text{eff}}^{\text{p}}$) fields and (b) shear strain (ε_{s}) fields of the 2024Al-T4 alloy targets after the 1st to 5th impact. The black dots in figure (b) mark locations for EBSD characterization in Fig. 11(a–d).

remains approximately the same for multiple impacts (Figs. 7 and 12).

The effective plastic strain ($\varepsilon_{\text{eff}}^{\text{p}}$) can be calculated with [60]

$$\varepsilon_{\text{eff}}^{\text{p}} = \int_0^t \left(\frac{2}{3}\dot{\varepsilon}_{ij}^{\text{p}}\dot{\varepsilon}_{ij}^{\text{p}}\right)^{\frac{1}{2}} \mathrm{d}t, \tag{7}$$

where $i, j = x, y$. t refers to time, and $\dot{\varepsilon}_{ij}^{\text{p}}$ is the plastic strain rate. $\dot{\varepsilon}_{ij}^{\text{p}}$ is equal to the total strain rate ($\dot{\varepsilon}_{ij}$) minus the elastic part ($\dot{\varepsilon}_{ij}^{\text{e}}$). $\varepsilon_{\text{eff}}^{\text{p}}$ accumulates continuously as the number of impacts increases (Fig. 14(a)), consistent with the microhardness measurements (Fig. 8). Pronounced $\varepsilon_{\text{eff}}^{\text{p}}$ is distributed mainly at a thin layer ($< \sim 4$ mm) adjacent to the crater edges, and decays rapidly to zero at far-field regions. The maximum $\varepsilon_{\text{eff}}^{\text{p}}$ increases from 1.29 to 1.72 for the 1st to 5th impacts. In addition, the maximum $\varepsilon_{\text{eff}}^{\text{p}}$ appears approximately at the crater bottom. The temperature field can then be obtained according to Eq. (6), and resembles the $\varepsilon_{\text{eff}}^{\text{p}}$ field. The temperature rise decays rapidly to zero along the radial direction (~ 1 mm away from the crater wall). Upon the first impact, the average temperature rise ($\overline{\Delta T}$) over the material elements in contact with the projectile increases with increasing time, and reaches a maximum of 177°C at the end of impact, yielding a time-average of ~ 130°C. This minor temperature rise is expected to have negligible effect on the mechanical properties and thus ballistic impact responses of the 2024Al-T4 alloy [61].

The shear strain (ε_{s}) is calculated as [62]

$$\varepsilon_{\text{s}} = \frac{1}{2}\left(\frac{\partial U}{\partial y} + \frac{\partial V}{\partial x}\right), \tag{8}$$

where U and V are displacements along the x and y directions, respectively.

Fig. 14(b) shows the shear strain fields around the crater. Similar to $\varepsilon_{\text{eff}}^{\text{p}}$, ε_{s} increases with increasing number of impacts and is localized in a thin layer adjacent to the crater edges as well. The maximum shear strain increases from 1.54 to 2.01 for the 1st to 5th impacts. However, the ε_{s} field exhibits different fea-

tures from the $\varepsilon_{\text{eff}}^{\text{p}}$ field. The ε_{s} maximum does not occur at the crater bottom, but at the arc-shaped region of the crater, consistent with the observed grain distortion there (Fig. 9(d)). In fact, the ε_{s} values at the crater bottom remain low after all the five impacts (0.25–0.30), indicating that the crater bottom region is subjected mainly to compression deformation. This explains why macroscopic DTs are not found at the crater bottom despite a high strain rate there ($\sim 4 \times 10^5$ s^{-1}). The regions for the EBSD characterization in Fig. 11(a–d) are marked by black dots in Fig. 14(b). The shear strains in the four regions are 0.75, 1.60, 1.14 and 0.76, respectively. For the 1st impact or sample 1, twin-like DBs are formed in the sample driven by shear. However, the accumulated shear strain is not sufficient for the formation of macroscopic DTs, and twin-like DBs remain eventually. With increasing number of impacts, shear strain accumulates continually in the arc-shaped region of the crater, and induces deformation twinning when it exceeds a critical value. Meanwhile, low angle GBs of DBs are driven by shear to rotate around the axis $\langle 111 \rangle$ [58]. With increasing distance from the crater edge, ε_{s} and strain rate both decrease significantly and macroscopic DTs are absent. Therefore, a critical ε_{s} required for the formation of macroscopic DTs in 2024Al-T4 alloys can be identified between 1.1 and 1.6 at the strain rates involved ($\sim 10^5$ s^{-1}).

4. Conclusions

Multiple ballistic impacts are carried out on the 2024Al-T4 alloy by spherical projectiles with a 5-mm diameter at ~ 400 m s^{-1}. Our main conclusions are as follows.

(1) An increase in the number of impacts gives rise to a minor increase in crater diameter, but a significant increase in crater depth and crater volume, all following a power law. Such power-law relations can help evaluate service safety and optimize structural design of protection structures under multiple impacts.

(2) Strain hardening leads to microhardness increase and a reduced rate of increase in crater depth with increasing number of impacts. Deformation bands and deformation twins are produced by impact as a result of spontaneous dislocation self-pinning and tangling under high strain-rate and large shear deformation. Macroscopic deformation twins are observed for the first time under ballistic impacts by virtue of accumulated shear strain at the arc-shaped region of crater.

(3) An FEM model is optimized to predict crater morphology, effective plastic strain and shear strain induced by multiple impacts, and the simulations agree well with the experimental observations. A critical shear strain required for the formation of macroscopic deformation twins in 2024Al-T4 alloys may be identified between 1.1 and 1.6 at the strain rates involved ($\sim 10^5$ s^{-1}).

Declaration of Competing Interest

The authors declare that they have no known competing financial interests or personal relationships that could have appeared to influence the work reported in this paper.

Acknowledgments

References

[1] Q. Zhang, Y.M. Zhu, X. Gao, Y.X. Wu, C. Hutchinson, Nat. Commun. 11 (1) (2020) 1–8.
[2] J.L. Zhang, B. Song, Q.S. Wei, D. Bourell, Y.S. Shi, J. Mater. Sci. Technol. 35 (2) (2019) 270–284.
[3] Y. Li, Y. Jiang, B. Liu, Q. Luo, B. Hu, Q. Li, J. Mater. Sci. Technol. 65 (2021) 190–201.
[4] Y. Li, B. Hu, B. Liu, A.M. Nie, Q.F. Gu, J.F. Wang, Q. Li, Acta Mater. 187 (2020) 51–65.
[5] X.C. Xu, D.X. Liu, X.H. Zhang, C.S. Liu, D. Liu, J. Mater. Sci. Technol. 40 (2020) 88–98.
[6] M.A. Meyers, Dynamic behavior of materials, John Wiley & Sons, 1994.
[7] A.A. Tiamiyu, A.Y. Badmos, A.G. Odeshi, J.A. Szpunar, Mater. Sci. Eng. A 708 (2017) 492–502.
[8] S.J. Perez-Bergquist, G.T. Gray III, E.K. Cerreta, C.P. Trujillo, A. Perez-Bergquist, Mater. Sci. Eng. A 528 (29–30) (2011) 8733–8741.
[9] Z. Rosenberg, G. Luttwak, Y. Yeshurun, Y. Partom, J. Appl. Phys. 54 (5) (1983) 2147–2152.
[10] Y.G. Wang, M.L. Qi, H.L. He, L.L. Wang, Mech. Mater. 69 (1) (2014) 270–279.
[11] T.T. He, Y. Xiong, Z.Q. Guo, L.F. Zhang, F.Z. Ren, A.A. Volinsky, J. Mater. Sci. Technol. 27 (9) (2011) 793–796.
[12] X.Q. Wu, Q.Y. Yin, C.G. Huang, J. Appl. Phys. 118 (17) (2015) 173102.
[13] L. Zhen, G.A. Li, J.S. Zhou, D.Z. Yang, Mater. Sci. Eng. A 391 (1–2) (2005) 354–366.
[14] Y.C. Ye, P.J. Li, L.S. Novikov, V.S. Avilkina, L.J. He, Acta Mater. 58 (7) (2010) 2520–2526.
[15] X.P. Liang, H.Z. Li, L. Huang, T. Hong, B. Ma, Y. Liu, T. Nonferr. Metal. Soc. 22 (6) (2012) 1270–1279.
[16] K. Tanaka, M. Nishida, N. Takada, Int. J. Impact Eng. 33 (1–12) (2006) 788–798.
[17] Z.G. Zhang, S.G. Shen, H.C. Song, D.X. Zhang, J. Mater. Sci. Technol. 14 (3) (1998) 265–268.
[18] Y. Itagaki, H. Tamura, Y. Watanabe, K. Taniyama, A. Takashima, Int. J. Impact Eng. 123 (2019) 38–47.
[19] J.Z. Lai, X.J. Guo, Y.Y. Zhu, Int. J. Impact Eng. 84 (2015) 1–12.
[20] J.T. Gomez, A. Shukla, Int. J. Impact Eng. 25 (10) (2001) 965–979.
[21] L. Zhu, D. Faulkner, Mar. Struct. 9 (7) (1996) 697–720.
[22] L. Zhu, K.L. Guo, Y.G. Li, T.X. Yu, Q.W. Zhou, Int. J. Impact Eng. 114 (2018) 123–132.
[23] K.L. Guo, L. Zhu, Y.G. Li, T.X. Yu, A. Shenoi, Q.W. Zhou, Compos. Struct. 200 (2018) 298–305.
[24] P.K. Jena, B. Mishra, K.S. Kumar, T.B. Bhat, Mater. Des. 31 (7) (2010) 3308–3316.
[25] M.B. Karamış, A.A. Cerit, F. Nair, Wear 261 (7–8) (2006) 738–745.
[26] B.Q. Li, M.L. Sui, S.X. Mao, J. Mater. Sci. Technol. 27 (2) (2011) 97–100.
[27] S. Xue, Z. Fan, Y. Chen, J. Li, H. Wang, X. Zhang, Acta Mater. 101 (2015) 62–70.
[28] F. Zhao, L. Wang, D. Fan, B.X. Bie, X.M. Zhou, T. Suo, Y.L. Li, M.W. Chen, C.L. Liu, M.L. Qi, et al., Phys. Rev. Lett. 116 (7) (2016) 075501.
[29] M.A. Khan, Y. Wang, A. Malik, F. Nazeer, G. Yasin, W.Q. Khan, T. Ahmad, H. Zhang, Arch. Civ. Mech. Eng. 19 (2019) 1484–1496.
[30] Y.L. Guo, Q. Luo, B. Liu, Q. Li, Scripta Mater. 178 (2020) 422–427.
[31] H.W. Chai, Z.L. Xie, X.H. Xiao, H.L. Xie, J.Y. Huang, S.N. Luo, Int. J. Plasticity (2020) 102730.
[32] B.X. Bie, S. Chen, T. Sun, K. Fezzaa, J.Y. Huang, S.N. Luo, Carbon 172 (2021) 781–790.
[33] R.G. Buchheit, R.K. Boger, M.C. Carroll, R.M. Leard, C. Paglia, J.L. Searles, Jom 53 (7) (2001) 29–33.
[34] J.C. Cheng, H.W. Chai, G.L. Fan, Z.Q. Li, H.L. Xie, Z.Q. Tan, B.X. Bie, J.Y. Huang, S.N. Luo, Carbon 170 (2020) 589–599.
[35] C.W. Hirt, A.A. Amsden, J.L. Cook, J. Comput. Phys. 14 (3) (1974) 227–253.
[36] G.R. Cowper, P.S. Symonds, Technical Report, Div. Appl. Math., Brown Univ., 1957.
[37] R. Goncharov, V. Zuzov, in: IOP Conf. Ser.: Mater. Sci. Eng., 963, 2020, p. 012007.
[38] L.E. Murr, E.A. Trillo, A.A. Bujanda, N.E. Martinez, Acta Mater. 50 (1) (2002) 121–131.
[39] S.P. Marsh, LASL shock Hugoniot data, 5, Univ. of California Press, 1980.
[40] F. Xi, K. Jin, L.C. Cai, H.Y. Geng, Y. Tan, J. Li, J. Appl. Phys. 117 (18) (2015) 185901.
[41] D. Koschny, E. Grün, Icarus 154 (2) (2001) 391–401.
[42] A. Suzuki, S. Hakura, T. Hamura, M. Hattori, R. Hayama, T. Ikeda, H. Kusuno, H. Kuwahara, Y. Muto, K. Nagaki, et al., J. Geophys. Res. Planet. 117 (E8) (2012).
[43] J.P. Ponthot, L. Adam, Mec. Comput. 23 (2004) 59–78.
[44] D. Rittel, L. Zhang, S. Osovski, J. Mech. Phys. Solids 107 (2017) 96–114.
[45] H.T. Li, W.D. Fei, D.Z. Yang, Mater. Sci. Eng. A 333 (1–2) (2002) 377–379.
[46] W.X. Cao, Y.F. Wang, P.Y. Zhou, X.B. Yang, K. Wang, B.J. Pang, R.Q. Chi, Z.Q. Su, Int. J. Mech. Sci. 163 (2019) 105097.
[47] X.K. Ma, Z. Chen, D.L. Zhong, S.N. Luo, L. Xiao, W.J. Lu, S.L. Zhang, J. Mater. Sci. Technol. 75 (2021) 27–38.
[48] B.X. Bie, J.Y. Huang, B. Su, L. Lu, D. Fan, T. Sun, K. Fezzaa, M.L. Qi, S.N. Luo, Mater. Sci. Eng. A 664 (2016) 86–93.
[49] Y.L. Guo, B. Liu, W. Xie, Q. Luo, Q. Li, Scr. Mater. 193 (2021) 127–131.
[50] J.Y. Liu, J.Q. Xiang, C. Li, L. Lu, Z.Y. Zhong, S.N. Luo, Mater. Sci. Technol. (2020) 1–6.
[51] N. Zolotorevsky, E. Ushanova, I. Brodova, A. Petrova, N. Ermakova, J. Alloy. Compd. 857 (2021) 158298.
[52] L.E. Murr, A. Ayala, C.S. Niou, Mater. Sci. Eng. A 216 (1–2) (1996) 69–79.
[53] D.K. Qi, M.X. Tang, L. Lu, F. Zhao, L. Wang, S.N. Luo, J. Mater. Sci. 54 (5) (2019) 4314–4324.
[54] Q. Luo, Y.L. Guo, B. Liu, Y.J. Feng, J.Y. Zhang, Q. Li, K. Chou, J. Mater. Sci. Technol. 44 (2020) 171–190.
[55] Y.P. Pang, Q. Li, Scr. Mater. 130 (2017) 223–228.
[56] Y.P. Pang, Q. Li, Int. J. Hydrogen Energy 41 (40) (2016) 18072–18087.
[57] Q. Luo, J.D. Li, B. Li, B. Liu, H.Y. Shao, Q. Li, J. Magnes. Alloy. 7 (1) (2019) 58–71.
[58] S.B. Jin, K. Zhang, R. Bjørge, N.R. Tao, K. Marthinsen, K. Lu, Y.J. Li, Appl. Phys. Lett. 107 (9) (2015) 091901.
[59] Y.P. Pang, D.K. Sun, Q.F. Gu, K.C. Chou, X.L. Wang, Q. Li, Cryst. Growth Des. 16 (4) (2016) 2404–2415.
[60] X. Zhang, Z. Chen, Y. Liu, The material point method: A continuum-based particle method for extreme loading cases, Academic Press, 2016.
[61] O.S. Lee, H. Choi, H. Kim, J. Mater. Sci. Technol. 25 (1) (2011) 143–148.
[62] J.T. Xing, Fluid-Solid interaction dynamics: Theory, variational principles, numerical methods, and applications, Academic Press, 2019.